Hindawi Publishing Corporation
International Journal of Aerospace Engineering
Volume 2016, Article ID 7928347, 15 pages
http://dx.doi.org/10.1155/2016/7928347

Research Article

Modeling of Particle Trajectory and Erosion of Large Rotor Blades

Adel Ghenaiet

Faculty of Mechanical and Process Engineering, University of Sciences and Technology (USTHB), BP 32, El-Alia, Bab-Ezzouar, 16111 Algiers, Algeria

Correspondence should be addressed to Adel Ghenaiet; ag1964@yahoo.com

Received 5 July 2015; Revised 5 November 2015; Accepted 16 November 2015

Academic Editor: Shaoping Wang

When operating in hostile environments, engines components are facing a serious problem of erosion, leading to a drastic drop in aerodynamic performance and life-cycle. This paper outlines the modeling and simulation of particle trajectory and erosion induced by sand particles. The governing equations of particle dynamics through the moving of large rotor blades are introduced and solved separately from the flow field by using our in-house particle tracking code based on the finite element method. As the locations of impacts are predicted, the erosion is assessed by semiempirical correlations in terms of impact conditions and particle and target surface characteristics. The results of these computations carried out for different concentrations of suspended dust (sand) cloud generated at takeoff conditions reveal the main areas of impacts with high rates of erosion seen over a large strip from the blade suction side, around the leading edge and the pressure side of blade. The assessment of the blade geometry deterioration reveals that the upper corner of blade suffers from an intense erosion wear.

1. Introduction

Aeroengines manipulating airflows laden by dust or volcanic ash suffer from extreme erosion wear, especially the front components. Inevitably, a great deal of dust, generated by a ground vortex that has the capability of picking up particles from the ground, enters the engine. In addition, the fine particles of dust cloud generated by rotor turning remain suspended for a considerable time, and when the blades move they are continually bombarded by the entrained particles [1]. In these circumstances, erosion is often seen on the leading edge as well as the aft of rotor blade body, thus leading to premature stall and producing a sudden change in torque and a rise in required power [2]. The role of erosion has been well recognized in turbomachinery applications, where the damage is evident in pitting on the blade leading edge and trailing edge and ensues in increased surface roughness [3]. Predominantly, in this context, erosion by solid particles and other particulates have shown detrimental effects on the aerodynamics of blades and life-cycle. One of the main effects of deterioration and fault is the modification of compressor and turbine performance maps [4] and subsequently the degradation of engine performance.

Sage and Tilly [5] were among the early researchers who attempted to quantify the erosion in turbomachinery, and since the past decades, this phenomenon has been the subject of many analytical and experimental investigations. Hussein and Tabakoff [6, 7] were the first to examine the role of particle material, density, and size on impacts locations and rebounds in 3D particle trajectory calculations through axial flow turbomachines. Later, Hamed and Fowler [8] demonstrated that, within twisted vanes, 3D particle trajectories are greatly influenced by the countering of hub and tip for different particle sizes. Hamed and Tabakoff [9] developed a methodology to predict blade surface erosion using the statistical impact data computed from the particle trajectory simulations and the correlations derived from erosion test results, which have been widely used in both axial and radial turbomachinery for automotive and gas turbine applications.

Early studies on high-pressure compressors [10, 11] and fans [12] atmospheric erosive regimes indicated that rotor-blade erosion occurred over the outer 50% of blade span.

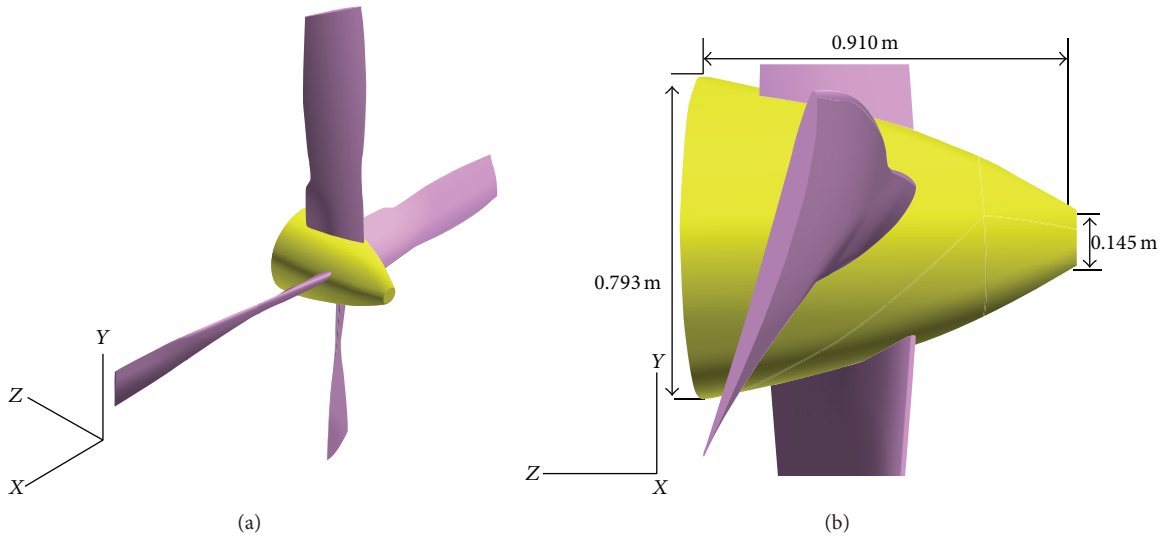

Figure 1: (a) Straight twisted four blades propeller. (b) Spinner and blades.

Balan and Tabakoff [11] studied experimentally the effects of sand ingestion on an axial flow compressor and found severe erosion of blade leading edge which increased the flow incidence that shifted the pressure rise coefficient and efficiency. Ghenaiet et al. [12, 13] found an increased tip to casing clearance and a reduction of blade chord in a high-speed axial fan following sand ingestion, and also noticed a 10% drop in efficiency and pressure rise coefficient due to blade leading edge blunting and erosive wear over the upper corner of blade. Hamed et al. [14] have reviewed in the detail the erosion and deposition in turbomachinery and the associated performance degradation of both aeronautical and ground based gas turbines. More recently, Ghenaiet [15] presented numerical results of erosion through the front compression stage of a turbofan, revealing the impact frequency, rates of erosion and critical areas of extreme erosion. Also, Schrade et al. [16] investigated numerically and experimentally the erosive change of a compressor blade shape based on different amounts of standardized Arizona test dust.

According to the literature, the study of erosion is still challenging due to numerous factors of complex interaction influencing the erosion process. These include flow conditions, geometry and material of blades, impact conditions, type of erodent, synergy of different erodents and exposure time. Moreover, most of the researches concentrated on compressors and turbines, but propellers practically received less interest. Therefore, further studies of particle dynamics and erosion facing open rotor blades (propellers), more susceptible to manipulate airflows laden by solid particles, are required to foresee the critical areas prone to erosion wear and subsequent blade shape deterioration. As noticed, hitherto there is no satisfactory protection for the leading edge even with stainless-steel coating [2].

This present study is a contribution to tackle the problem of erosion of large open rotor blades (propeller) at takeoff operation. For this purpose, our in-house particle tracking code [12, 13, 15] was adapted to this configuration of turbomachinery. The flow data were obtained separately and then followed the computations of particle trajectories and the determination of locations and conditions of impacts which served in evaluating the erosion rates and in the assessment of blade profile deterioration. The obtained results considering sand (quartz) particle (0–1000 mm) depict erosion wear that increases with particle concentration and reveal the main eroded areas along the fore of blade suction side and leading edge as well as the spinner.

2. Case Study

This study concerns a model of straight twisted propeller (Figure 1(a)) with large four blades, of a diameter equal to 4.117 m, made from aluminum alloy and operated by a single shaft gas turbine running at a constant speed of 13820 rpm via a gear box of a reduction ratio of 1/13.52. The overall length of spinner made from composite material (Figure 1(b)) is 0.91 m and its maximum diameter is 0.793 m. The 3D geometry was reconstituted by stacking different profiles from root to tip according to the measured blade twist. At the takeoff operation, the blade setting angle is equal to 25 deg measured between the blade chord and the tangential direction (at the reference radius $R75$), and the advance speed is equal to 74.6 m/s (145 knots).

3. Computational Domain

The computational domain (Figure 2) contains a rotating domain modeling one blade passage and a stationary domain consisting of extended inlet and outlet domains and a top domain over the propeller tip. At the pitchwise sides of these domains, the periodic boundary condition is used.

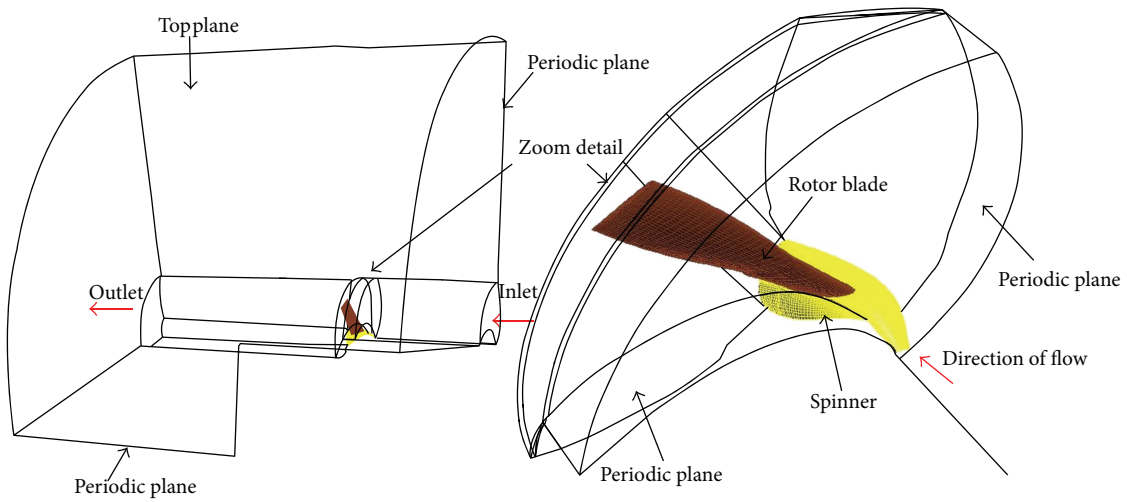

Figure 2: Full computational domain showing the rotor blade and the spinner and the boundary conditions.

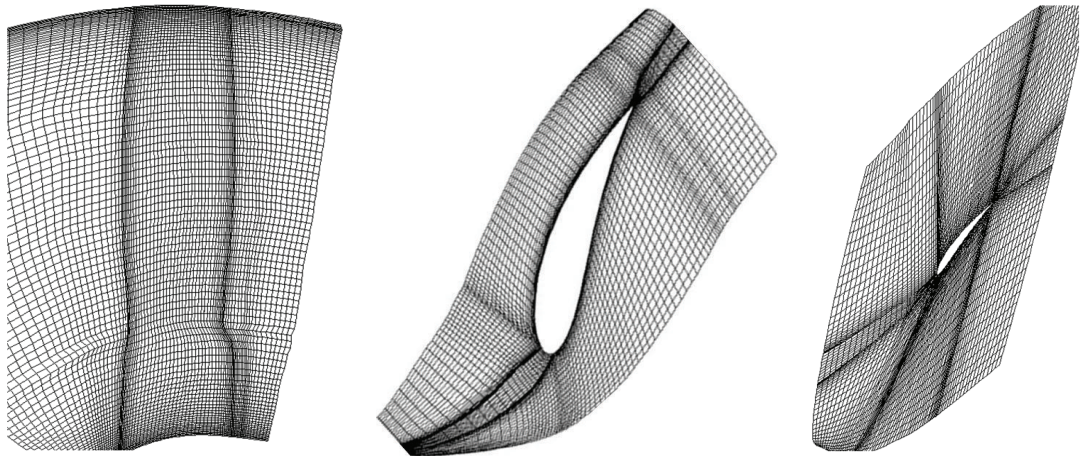

(a) (b) (c)

Figure 3: Grids of H type plotted from hub to tip meridional plane (a) and over hub and $R75$ planes (b, c).

Many of the difficulties encountered when applying CFD to an open rotor (a propeller) arise due to removal of casing existing in a conventional turbomachinery. The distances at upstream and downstream of the rotating domain are taken to sufficiently prevent any influence of the finite domain size on the aerodynamic performance of rotor. The mesh in the radial direction was sufficiently extended to capture the propeller stream-tube and to minimize the effects of the finite domain size. The locations of the rotating domain interfaces planes and the distances upstream and downstream of the spinner are critical and have a strong influence upon flow solution. Accordingly, the sizes of upstream, downstream, and top domains were examined to get a compromise with the particle trajectories computations that used the same grids. The distances upstream and downstream of the blade were taken as equal to $0.5c$ (c: axial mean chord), and the extended distances for inlet, outlet, and top were equal to $1.5D$, $2.5D$, and $3D$ (D: rotor diameter), respectively.

The rotating domain was meshed by CFX-TurboGrid, whereas the stationary domain used CFX-TASCgrid. Multi-block H type meshes were generated (Figure 3) with dense clustering around the blade in order to guarantee a better boundary layer resolution, in addition to the refinements near hub and tip. The transition from the rotating to stationary domain occurred with a smooth change of computation cells, to make sure that the conservative quantities are satisfied. As far as the quality of the meshes was concerned, some parameters have to be checked such as grid orthogonality characterized by a skew angle (between vertices) between 15 and 120 deg, minimum positive volumes, and cell aspect ratio not exceeding 100. The effect of computational domain mesh size was investigated for both the rotating domain and the stationary separately. To study the effect of propeller mesh on the propulsive efficiency, seven grids were used and the propulsive efficiency was assessed. The number of cells from one grid to another was scaled by a factor of 1.05 in all

three directions. As a conclusion, about 450000 nodes were selected for the rotor domain. The influence of the mesh size of the stationary domain was explored by testing three different grids. Because of the computing time that might increase drastically for the third large grid size, it was decided to keep the first grid size of 350000 nodes for the stationary domain.

The adopted turbulence closure model for RANS equations is the k-ω model (Shear Stress Transport) with an automatic near-wall treatment [17]. This latter automatically switches from wall functions to a low-Reynolds near-wall formulation as the mesh is refined, but this cannot be guaranteed in most applications at all walls and some regions, for instance, blade junction to hub. This turbulence model was chosen for several reasons. First, the effects of free stream turbulence and surface roughness are easily included in the model [18]. Second, the transition can be calculated using the low-Reynolds number version of the model [19]. Third, Menter has shown that this model does well for flows with adverse pressure gradients [20, 21]. Finally, it should behave well numerically since it avoids using the distance to the wall and the complicated damping functions requiring a high computer power. Near walls, nodes were positioned in such a way that the value of $y^+ = \rho y_p u_t/\mu_f$, $u_t = V_f\sqrt{f/2}$ (V_f is flow velocity), and the friction factor is based on a flat plate $f = 0.025\mathrm{Re}_x^{-0.1428}$. For an average value $y^+ = 40$, the last relation is simplified to $y_p = 357.77c\mathrm{Re}_c^{-0.92}$, based on an average blade chord and used to position the near-wall first lines. In order to cover regions of high Reynolds number, the maximum flow velocity at the blade tip was used in the previous relation.

4. Flow Field Solution

Particle trajectory simulations through the components of a turbomachine are based on the numerical integration of particle equations of motion, which require the 3D flow solution of the RANS (Reynolds averaged Navier-Stokes) equations for turbulent flows by means of CFD (computational fluid dynamics) tools. In this study, the flow solution used the code CFX-TASCflow [17] which is a finite volume based solver. A sliding interface is used to connect two regions together (different frames of reference), in order to account for the change in the frame of reference and support steady-state predictions in the local frame. The interface sides must be a surface of revolution and sweep out the same surface of revolution and account internally for the pitch change by scaling up or down the local flows as they cross the interface. The boundary conditions used are periodic boundaries applied at one pitch of the blade, whereas symmetry is applied at the intersection planes joining on the axis of rotation. A rotating wall at the speed of 107 rd/s is selected for the blade and the spinner. A constant total pressure of 104541.4 Pa and temperature 288.15 K are applied at the inlet of the upstream domain, whereas at the outlet a static pressure of 101300 Pa is set at a single face near the top. A free stream velocity of 74.6 m/s is set over the top domain. At the inlet, the turbulence intensity was set at 5% and a value of turbulent viscosity μ_t was evaluated using Wilcox's model [18, 19].

The flow field within the blades is obtained in a relative frame and assumed to be steady. By adopting the approach of a frozen rotor, the stationary and rotating frames have fixed positions during the calculations. In the finite volume approach [17], all the diffusion terms are evaluated by summation of the derivatives of the shape function. The advection terms are computed by using a linear profile scheme (LPS) and a mass weighted skew upstream differencing scheme, which incorporate the physical advection correction. Initially the robust upwind scheme was used and then changed to a linear profile scheme for producing better results. The local time step was based on the tip blade chord and flow velocity. To ensure a good convergence, two criteria were considered: an RMS residual less than 10^{-5} and an imbalance in the conservation equations less than 10^{-2}, which are usually sufficient for an adequate convergence in most of the engineering applications. The RMS residual is the square root of the mean of all square residuals throughout the computational domain. The target imbalance for the conservation equations is used to ensure that the global balances are met, which is specified as the maximum fractional imbalance equal to the ratio of the subdomain imbalance and the maximum one over all subdomains.

As a result, Figure 4 plots the vectors of flow velocity near the blade hub, at $R75$ and blade tip, showing an increase in velocity with blade span. The relative flow velocity increases from the blade leading edge till a critical point over the suction side and afterwards tends to reduce toward the trailing edge. As noticed, the shape of spinner and its extended contour cause a flow blockage that increases the axial velocity and reduces the flow incidence onto the leading edge. At the takeoff operating regime, the relative Mach number is shown to increase along the blade span (Figure 5) to reach higher values beyond $R75$, but its value at blade tip does not exceed 0.712. Also, the relative Mach number contours depict a wake area expanding behind the blade. As the static pressure over the lower surface of blade is larger than at the upper one and the surrounding, the flow tends to curl as being forced from a high-pressure region just underneath the tip of blade to a low-pressure region. As a result, there is a spanwise component of the flow from the tip toward the root causing the flow streamlines at the upper surface to bend toward the root. Similarly, on the lower surface, there is a spanwise component of flow from root to tip forcing the streamlines to bend towards the tip. These two streams combine at trailing edge and the velocity difference causes the air to roll up into a vortex just inboard. This mechanism is observed in the formation of vortices (Figure 6) detaching from the blade tip to follow helicoidal flow paths in the same direction of blade rotation, which later dissipates with the downstream distance.

5. Particle Dynamics

The basis for particle trajectory simulations in turbomachinery continues to be Eulerian and Lagrangian with one-way coupling between the particles and flow. The Lagrangian approach considers the tracking of individual particles from different starting positions, thus giving an ability to handle in more detail some physical aspects, such as the interaction

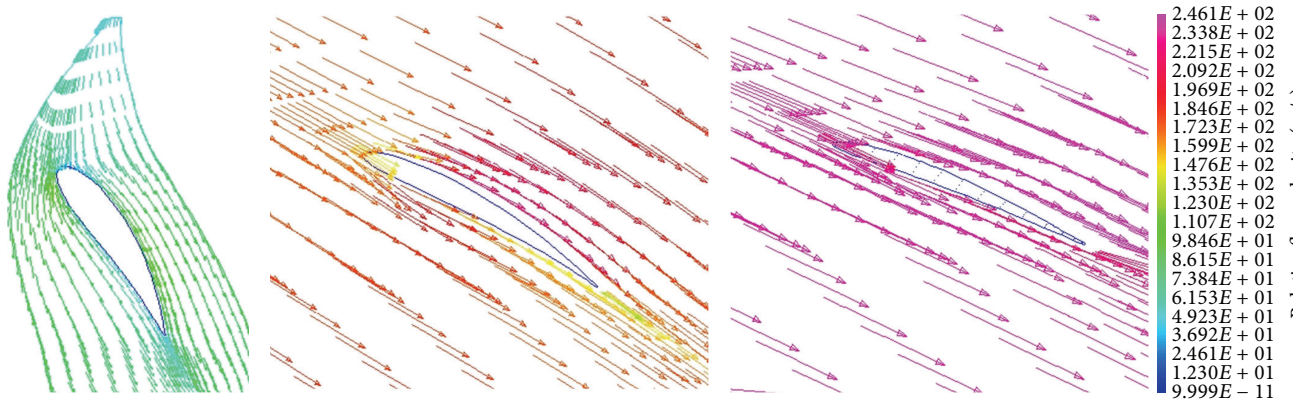

Figure 4: Relative flow velocity vectors: (a) near hub, (b) at $R75$, and (c) at blade tip.

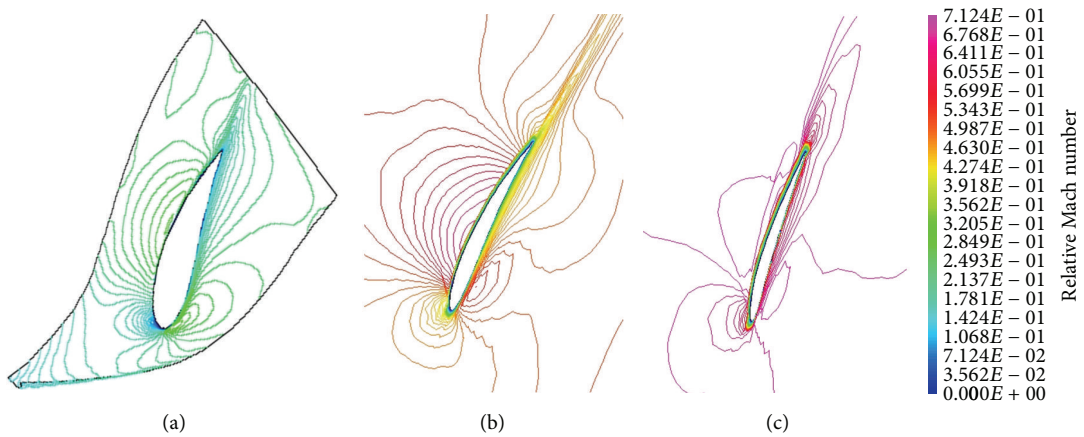

Figure 5: Relative Mach number (a) near hub, (b) at $R75$, and (c) at tip.

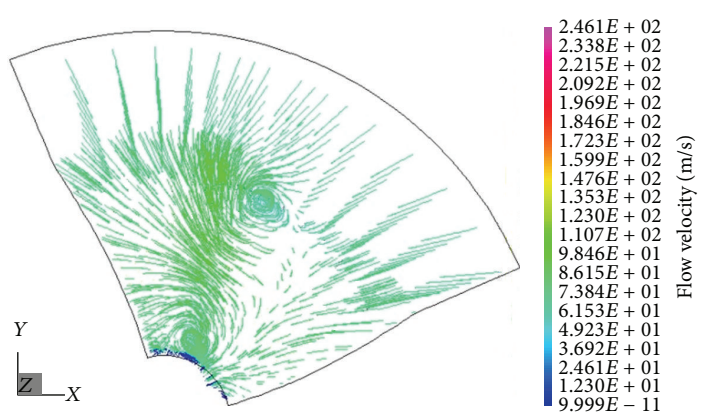

Figure 6: Counter-rotating vortex downstream of the rotor blade.

with walls. This approach is somewhat more economical since the effect of particle phase on the flow solution is neglected for very low volume fractions.

The particle trajectory equations are derived from the superposition of different involved forces, but in most particulate air flows the drag force is dominant. The general expression for the drag coefficient C_D is given (as below) according to Haider and Levenspiel [22], for Reynolds number from 0.01 to 2.6×10^5. For small Reynolds numbers (Re < 0.5), the viscous effect is dominating and this is referred to as the Stokes regime; $C_D = 24/\mathrm{Re}$. The constants A, B, C, and D depend on the particle shape:

$$\begin{aligned}
\vec{F}_D &= \frac{\pi}{8} d_p^2 \rho_f C_D \left(\overrightarrow{V_f} - \overrightarrow{V_p}\right) \left|\left|\vec{V}_f\right| - \left|\vec{V}_p\right|\right|, \\
C_D &= \frac{24}{\mathrm{Re}_p}\left(1 + A\mathrm{Re}_p^B\right) + \frac{C}{\left(1 + D/\mathrm{Re}_p\right)}, \\
\mathrm{Re}_p &= \frac{\rho_f}{\mu_f} d_p \left|\vec{V}_f - \vec{V}_p\right|.
\end{aligned} \tag{1}$$

If a particle is sufficiently large and there is a large velocity gradient, there will be a lift force called Saffman force due to fluid shearing forces, which depends on the particle based Reynolds number and the shear flow Reynolds number [23] as follows:

$$\begin{aligned}
\vec{F}_S &= \frac{\pi \rho_f}{8} d_p^3 C_{LS} \left(\vec{V}_f - \vec{V}_p\right) \times \nabla \vec{V}_f, \\
C_{LS} &= \frac{4.1126}{\sqrt{\mathrm{Re}_S}} f\left(\mathrm{Re}_p, \mathrm{Re}_S\right), \\
\mathrm{Re}_S &= \frac{\rho_f}{\mu_f} d_p^2 \left|\vec{\Omega}_f\right|.
\end{aligned} \tag{2}$$

The particle inertia forces, namely, the centrifugal and Coriolis forces, are derived from the second derivative of the vector position. By considering the drag and Saffman force as the main external forces, the following set of second-order nonlinear differential equations is derived:

$$\begin{aligned}
\frac{\partial^2 r_p}{\partial t^2} &= G\left(V_{fr} - V_{pr}\right) + r_p\left(\omega + \frac{V_{p\vartheta}}{r_p}\right)^2 + \frac{F_{Sr}}{m_p}, \\
\frac{\partial^2 \theta_p}{\partial t^2} &= G\frac{\left(V_{f\vartheta} - V_{p\vartheta}\right)}{r_p} - 2\frac{V_{pr}}{r_p}\left(\omega + \frac{V_{p\vartheta}}{r_p}\right) + \frac{F_{S\vartheta}}{r_p m_p}, \\
\frac{\partial^2 z_p}{\partial t^2} &= G\left(V_{fz} - V_{pz}\right) + \frac{F_{Sz}}{m_p}, \\
G &= \frac{3}{4 d_p}\frac{\rho_f}{\rho_p} \\
&\quad \cdot C_D \sqrt{\left|V_{fr} - V_{pr}\right|^2 + \left|V_{f\vartheta} - V_{p\vartheta}\right|^2 + \left|V_{fz} - V_{pz}\right|^2}.
\end{aligned} \tag{3}$$

Turbulence Effect. The fluctuating components corresponding to a particular eddy are obtained from the local turbulence properties. Turbulence effect is assumed to prevail as long as the particle-eddy interaction time (minimum between eddy lifetime and transit time, Brown and Hutchinson [24]) is less than the eddy lifetime. The eddy lifetime and dissipation length scale are estimated according to Shirolkar et al. [25]:

$$\begin{aligned}
t_e &= A\frac{k}{\varepsilon}, \\
l_e &= \frac{Bk^{3/2}}{\varepsilon}, \\
\frac{A}{B} &= \sqrt{1.5}.
\end{aligned} \tag{4}$$

The transit time scale is estimated from a linearized form of equation of motion given by Gosman and Ionnides [26]:

$$\begin{aligned}
t_r &= -\tau_p \mathrm{Ln}\left[1 - \frac{l_e}{\tau_p\left|\left|\overrightarrow{V_f}\right| - \left|\overrightarrow{V_p}\right|\right|}\right], \\
\tau_p &= \frac{24\rho_p d_p^2}{18\mu_f C_D \mathrm{Re}_p}.
\end{aligned} \tag{5}$$

Boundary Conditions. The boundary conditions implemented in the particle trajectory code include the interface between stationary frame and rotating frame, where the vector of particle velocity is decomposed into a tangential and a relative velocity. The tangential component is modified by adding the circumferential velocity, while the other components remain the same. At the periodical lateral sides, the velocity vector components are conserved while the tangential coordinate is modified by the angular shift. At the axis of revolution (condition of symmetry), for the velocity vector, a pure reflection is used. The impact physics is required to trace the particle trajectory after an impact with a surface, where the restitution coefficients (a measure of the kinetic energy exchange upon impact) are used to define variations in the magnitude and direction of a particle velocity. The impact angle β_1 is defined as the angle formed between the vector velocity of a particle at an impact point and its tangential component. In the course of particle trajectory computation, the restitution coefficients are estimated statistically based on the experimental values of mean and standard deviation (Tabakoff et al. [27]), given as polynomial regressions:

$$\begin{aligned}
\frac{V_{P2}}{V_{P1}} &= \sum_{i=0}^{4} a_i \beta_i^i, \\
\frac{\beta_{P2}}{\beta_{P1}} &= \sum_{i=0}^{4} b_i \beta_i^i.
\end{aligned} \tag{6}$$

Particle Distribution. The particle mass rate was obtained by multiplying the inlet air volume flow rate at the inlet by the mean value of particle concentration. The number and sizes of sand particles depend on the cumulative distribution

curve 0–1000 μm (of mean diameter and variance equal to 237.4 μm and 164.5 μm, resp.) and the specified concentration profile. In the present simulations, particle concentration was varied in between 10 and 500 mg/m^3. As sand particles were released randomly with size distribution from 0 to 1000 μm, an iterative procedure, involving particle number and size in addition to the radial and circumferential seeding positions, was repeated until a convergence in the total mass of particles.

Solving Procedure. The flow data at the grids nodes were used to interpolate for the local flow properties, in the course of particle trajectory integration based on the Runge-Kutta-Fehlberg seventh-order technique. The integration time step depends on the computational cells sizes and the local flow velocities. However, this time step is reduced within the integration procedure to keep the leading truncation error within the tolerance. If a particle interacts with an eddy, the interaction time is considered as the effective time step. Near a boundary condition, a more accurate time step is reevaluated to get an impact within a half-diameter distance. After an impact, the restitution coefficients are used and the derived particle fragmentation factor (based on experiments by Tan and Elder [28]) is considered.

The particle tracking algorithm is based on the finite element method which requires transforming a particle position into its local coordinates by solving nonlinear equations (7). If these values do not exceed unity, that means the particle is still in the same cell; otherwise the algorithm starts to check all surrounding cells and the cell increment for a specified directrix is used to update the exact cell:

$$x_p = \sum_{i=1}^{8} N_i x_i,$$
$$y_p = \sum_{i=1}^{8} N_i y_i, \tag{7}$$
$$z_p = \sum_{i=1}^{8} N_i z_i.$$

6. Erosion Assessment

This later depends on the physical properties of target surface and erodent, particle concentration and size, and the velocity and angle of impact. Finnie [29] attempted to develop the basic theoretical analysis of sand erosion based on Hertz's contact theory, but his model did not exactly predict the weight loss for high impact angles. Bitter suggested the mechanism of sand erosion which consists of deformation wear and cutting wear [30]. Bitter's model that accounts for erosion at all impact angles gives the sufficient prediction for both of ductile and brittle materials, but it is too complex. Neilson and Gilchrist [31] modified Bitter's model by assuming that the total erosion is an arithmetic combination of brittle and ductile contributions, and thus erosion loss can be predicted at intermediate impact angles. However, the resulting equations are still complex as requiring experimentally determined parameters. The most successful erosion prediction model used in turbomachinery was developed by Grant and Tabakoff [32, 33], based on erosion measurements of 2024 aluminum alloy at particle speeds of 61–183 m/s and sand (quartz) as abrasive particles (20–200 micron). This latter is implementing two mechanisms, one predominant at low impact angle and another at high impact angle, as follows:

$$E = K_1 f(\beta_1) V_{P1}^2 \cos^2\beta_1 \left(1 - R_\theta^2\right) + K_3 \left(V_{P1} \sin\beta_1\right)^4, \tag{8}$$

$$f(\beta_1) = 1 + CK\left(K_2 \sin\frac{90}{\beta_o}\beta_1\right), \qquad CK = \begin{cases} 1 & \beta_1 \le \beta_o \\ 0 & \beta_1 > \beta_o. \end{cases} \tag{9}$$

Erosion rate is expressed as the amount (milligram) of material removed per unit of mass (gram) of impacting particles. R_θ is the tangential restitution factor derived from (6); the unit of velocity should be in ft/s. The material constants $K_1 = 3.67 \times 10^{-6}$, $K_2 = 0.585$, and $K_3 = 6 \times 10^{-12}$ and the angle of maximum erosion $\beta_o = 20$ deg are available for aluminum based alloy.

It was shown by many authors that the erosion damage increases with particle size up to some plateau value. Further, the influence of particle size on erosion is more pronounced at higher particle velocities [32]. The effect of particle size was included to correct the predicted erosion rate based on semiempirical correlation (8). It should be noted that, for the spinner made from a composite material, the specific restitution coefficient and erosion correlation were adopted from the experiments due to Drensky et al. [34].

The local values of mass erosion (milligram) are calculated from the local erosion rates and then cumulated over a given mesh element surface A_e in order to compute the equivalent erosion rate expressed in mg/g/cm^2. This latter was interpolated for the same node sharing the elements faces to get the nodal value distribution, which served to plot the contours of equivalent erosion rates:

$$E_{\text{eq}} = \frac{1}{A_e \sum_1^{N_p} m_{p_i}} \sum_1^{N_p} m_{p_i} E_i. \tag{10}$$

The depth of penetration per a unit of time for an element face is calculated from the cumulative mass erosion of the given face. For the elements sharing the same node, the nodal values of penetration are estimated based on bilinear interpolation. As a result, the new coordinates are evaluated by knowing the normal vector and the depth of penetration at the given node. The assessment of blade geometry deterioration in terms of percentages of averaged reduction in blade

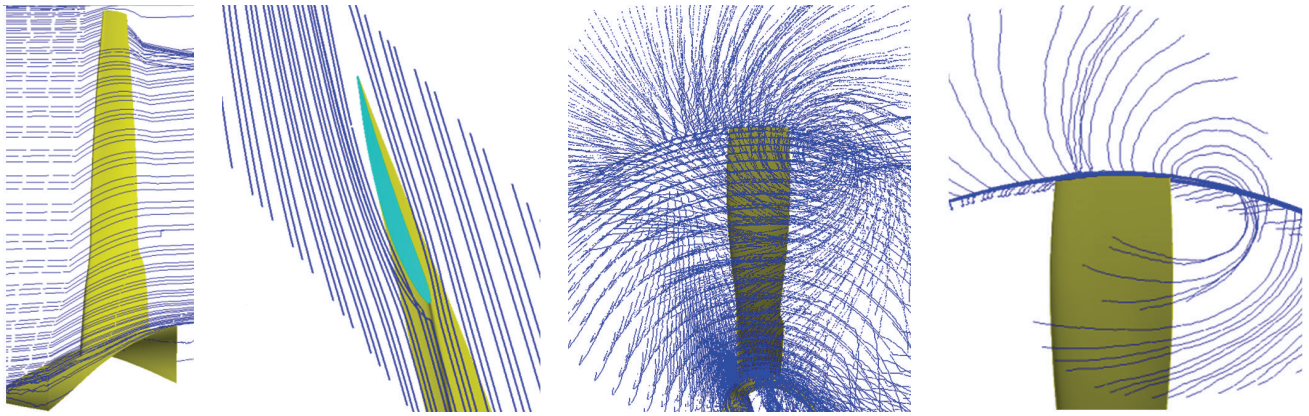

(a) (b) (c) (d)

Figure 7: Sample of sand particle (10 μm) trajectories: (a) streamwise from hub to shroud, (b) near the tip, (c) downstream of rotor blade, and (d) downstream of rotor blade reflecting particles crossing over the blade tip.

chord and blade thickness is based on the whole blade length as follows:

(i) Average reduction in blade chord:

$$\Delta c_{\text{av}}\,(\%) = 100\left[1 - \frac{1}{c_{\text{av}}h}\sum_{j=1}^{m}\delta c_j \cdot \delta h_j\right]. \tag{11}$$

(ii) Average reduction in blade thickness:

$$\Delta e_{\text{av}}\,(\%) = 100\left[1 - \frac{1}{e_{\text{av}}h}\sum_{j=1}^{m}\frac{1}{c_j}\sum_{i=1}^{n}\delta e \cdot \delta c_i\right]. \tag{12}$$

7. Results and Discussion

The air and particles experience different degrees of turning through the rotor blade depending on their sizes. The deviations from air flow paths increase with particle inertia to provoke repeated impacts with the various surfaces of rotor blade. Figure 7 shows samples of simulated particle trajectories corresponding to small size particles, for instance, 10 microns, which tend to follow the flow paths closely (Figure 7(a)) along the blade passage from hub to shroud. Many of them are shown to collide with the spinner with repeated impacts. At outer radii, these particles are deviated downward owing to the rotational flow structure emanating from the tip and also because of moving from a rotating frame to a stationary one. The other view around the blade near tip (Figure 7(b)) depicts small particles circulating around the blade, and many of them impact around the leading edge and bounce closely to hit another time the suction side. Due to the formation of flow vortices (Figure 6) downstream of the blade, these tiny particles tend to follow a helicoidal trajectory (Figure 7(c)) and are strongly influenced by the flow turbulence. Detailed Figure 7(d) describes the trajectories of particles arriving toward the tip of blade, showing particles being entrained by the vortex, and many others are centrifuged outward from the blade tip.

When inertia of particles becomes more important, such as the case of 250 microns, they deviate considerably from the flow streamlines as shown in Figure 8. Many of these large size particles impact spinner wall (Figure 8(a)) and hence are deflected upward to follow ballistic trajectories. Also, owing to high centrifugal forces imparted, these particles are seen to deviate towards outer radii. At exit from rotor, and because of changing from a rotating frame to a stationary one, the large particles are heavily deviated tangentially. As seen in Figure 8(b), after hitting the fore part of suction side, these particles are deflected and follow bowed trajectories. Detailed Figure 8(c) depicts trajectories of large sand particles when arriving around the outer blade radius; they are shown to be entrained over the blade tip and receive high centrifugation projecting them upward from the rotor. Even for these heavy particles, some of them are being entrained by the vortex causing them to deviate downward (Figure 8(c)) after crossing the rotor.

Figure 9 shows that all particle trajectories related to size distribution (0–1000 μm) released upstream of the rotor combine all the features related to small and large size particles. Large particles are shown to deviate upwards due to high imparted centrifugal forces as compared to the drag force. These particles are accelerated in the axial direction and then impact the spinner to be largely deflected. Sand particles after crossing the rotor blade are deviated considerably towards the tangential direction and are entrained by the vortex structure behind the rotor blade.

Figure 10 shows impacts induced by a reduced sample (for the sake of plots clarity) of sand particles of a random size distribution (0–1000 μm). As revealed, the region of maximum impact frequency and erosion rate appears on the hub portion and the spinner, in addition to a large band at the front suction side and the back of pressure side. Figure 10(a) shows that a large number of particles tend to impact around the leading edge of propeller blade, and many others hit the suction side over a large strip from the leading edge and bounce to reach the pressure side towards the mid of trailing

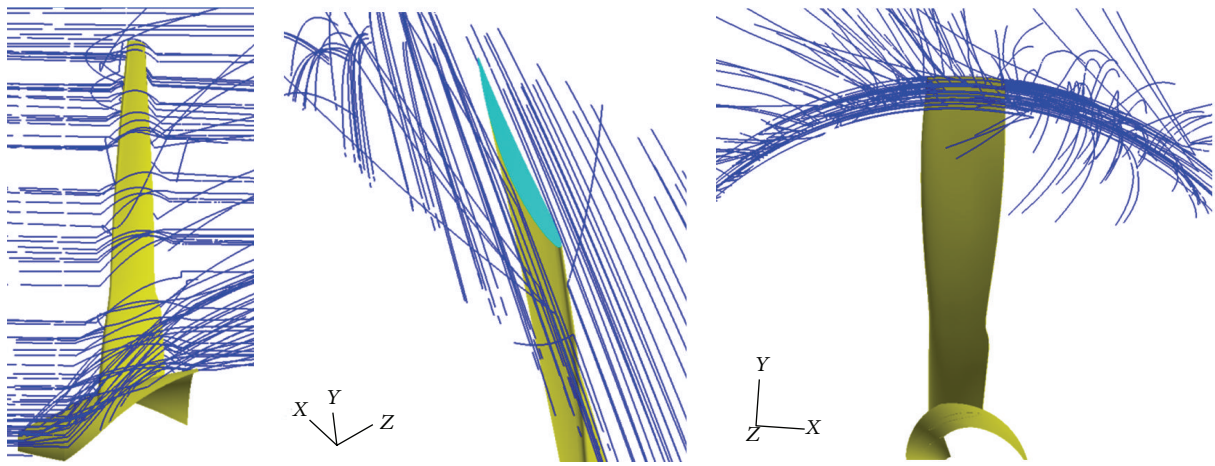

Figure 8: Sample of sand particle (250 μm) trajectories: (a) streamwise from hub to shroud, (b) near the tip, and (c) downstream of rotor blade reflecting particles crossing over the blade tip.

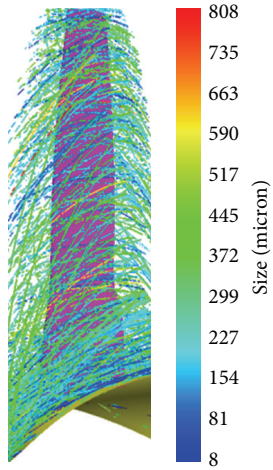

Figure 9: Sample of sand (0–1000 μm) particles trajectories crossing the rotor blade.

edge. Also, some particles are shown to impact around the trailing edge from suction side. Impacts on spinner are concentrated on the fore part, with a large crowd of particles seen along suction side at blade junction and around leading edge from both sides. Large impact velocities (Figures 10(b) and 11(b)) reaching a velocity of 223.5 m/s are predicted above the upper part and around the leading edge from both sides, owing to high flow velocities and rotation effect. As consequence, the high local rates of erosion are observed over the front part of suction side and around the leading edge from both sides (Figures 10(c) and 11(c)). The critical area of pronounced erosion is seen over the tip corner. Also there are regions of impacts towards the trailing edge from both sides.

The impacts frequency, the velocities, and angles of impacts and their distribution over the impacted surfaces strongly affect the erosion patterns, estimated by semiempirical equation (8). The values of mass erosion (mg) at discrete points of an element face are calculated based on the local erosion rates in mg/g and cumulated to compute the equivalent erosion levels in mg/g/cm^2. Figures 12 and 13 depict the equivalent erosion rates corresponding to a low concentration (10 mg/m^3) and a high concentration (500 mg/m^3) of sand particles. All figures show noticeable erosion wear of the blade leading edge from the root to tip related to particles arriving at high velocity and also because of spanwise twist of the rotor blade that changed effectively the angle of particle incidence. The areas of erosion wear are seen to expand towards the tip in a triangular pattern with a spot area over the tip corner. On the blade pressure side, erosion is seen from the leading edge, in addition to a region of low erosion rates towards the trailing edge. On the spinner, there is a large spread of erosion but with low rates. Practically, similar patterns of erosion are obtained for each concentration, but the local mass erosion rates differ. As expected for this large rotor blade, the actual equivalent rates of erosion are lower in comparison with, for instance, the front stages of an axial compressor, according to the numerical results obtained by Ghenaiet [15], and this because of moderate flow velocity related to low rotational speed and the relatively large blade size.

The estimated mass erosion and blade geometry deterioration after one hour of sand ingestion are presented in Table 1. It is clear that the material removal and geometry changes are related to the size and mass (concentration) of particles impacting the blade surfaces and duration of exposure. The eroded mass from the rotor blade and spinner (Figure 14) and the subsequent geometry deteriorations estimated as percentages reductions of chord, thickness, and blade length are plotted in Figure 15, depicting an increase with concentration. The erosion wear is manifested by a drastic reduction in blade chord towards the tip and

Table 1: Erosion parameters and geometry deterioration of one blade after one hour.

Erosion parameters	Different concentrations (mg/m^3) sand (0–1000 μm)						
	10	25	50	100	250	400	500
Sand particle rate (mg/s)	2.53	6.32	12.66	25.28	63.25	101.24	126.59
Ingested mass of sand (g)	9118.12	22751.19	45582.79	91002.2	227689.9	364483.2	455739.2
Erosion of blade (mg)	321.67	793.76	1568.49	3179.50	7820.65	12659.03	15734.07
Erosion of spinner (mg)	15.95	39.54	82.52	163.65	413.26	662.18	823.61
Reduction of chord at $R75$ (%)	$2.197E-03$	$6.34E-03$	$7.87E-03$	$1.62E-02$	$6.00E-02$	0.1029	0.1183
Reduction of chord at tip (%)	$4.449E-03$	$8.02E-03$	$1.28E-02$	$2.31E-02$	$7.62E-02$	0.1111	0.1503
Average reduction of $R75$ blade thickness (%)	$1.344E-02$	$4.774E-02$	$8.638E-02$	$1.636E-01$	$3.915E-01$	$6.485E-01$	$8.130E-01$
Average reduction of tip blade thickness (%)	$3.621E-02$	$7.169E-02$	$1.335E-01$	$3.766E-01$	1.365	1.954	2.321
Decrease of blade length (%)	$1.96E-05$	$2.37E-05$	$3.04E-05$	$5.57E-05$	$1.40E-04$	$2.071E-04$	$2.38E-04$

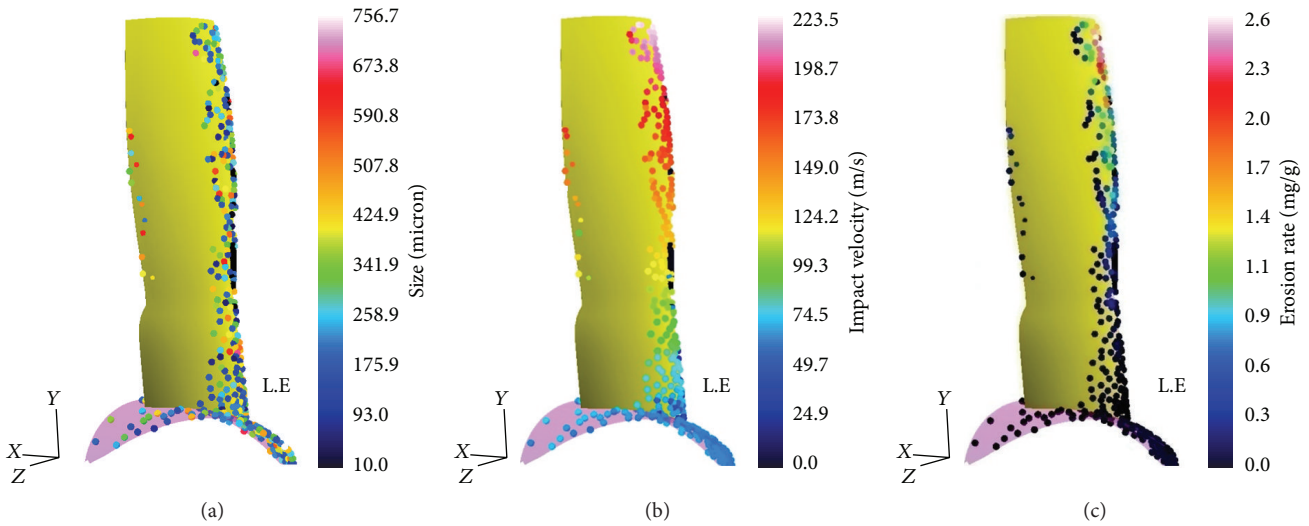

Figure 10: Sample of local impacts on suction side: (a) particles sizes (μm), (b) impact velocities (m/s), and (c) erosion rates (mg/g).

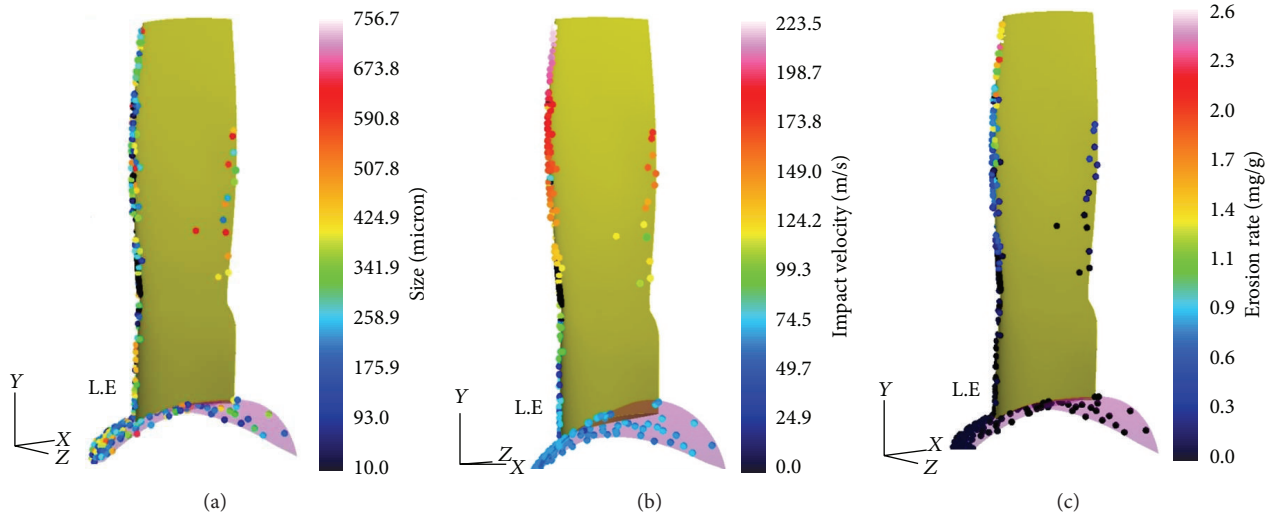

Figure 11: Sample of local impacts on pressure side: (a) particles sizes (μm), (b) impact velocities (m/s), and (c) erosion rates (mg/g).

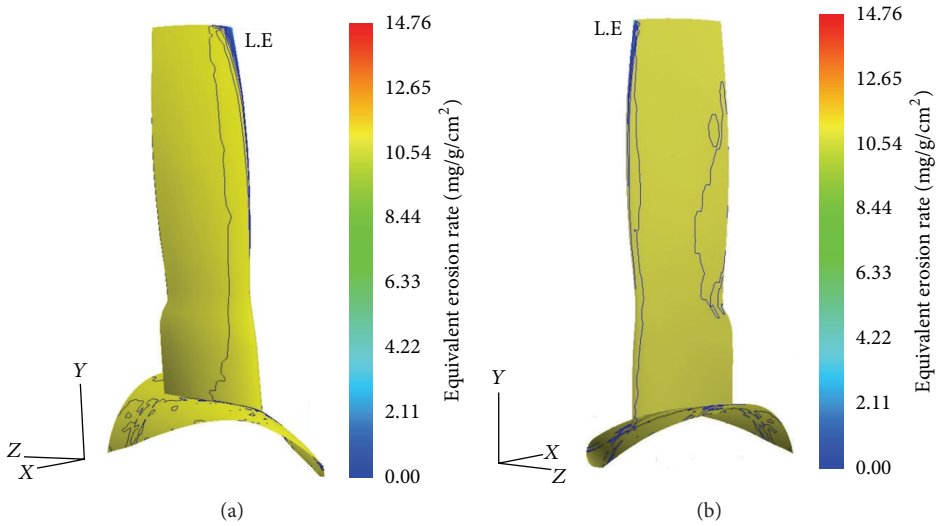

FIGURE 12: Equivalent erosion rates (mg/g/cm^2) at low concentration (10 mg/m^3): (a) Suction side and (b) pressure side.

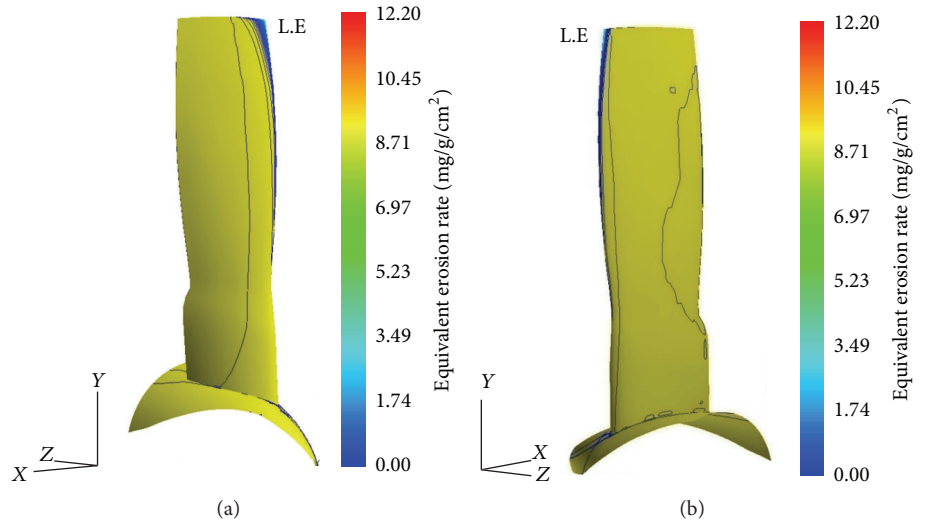

FIGURE 13: Equivalent erosion rates (mg/g/cm^2) at high concentration (500 mg/m^3): (a) Suction side and (b) pressure side.

a distortion (blunt) of leading edge, which are generally the main sources in the aerodynamic performance degradation. Accordingly, the mass erosion of one blade increases with particle concentration (between 10 and 500 mg/m^3) from 321.67 mg to 15734.07 mg, as illustrated in Figure 14(a). Also, the mass erosion of one quarter of spinner increases with particle concentration (between 10 and 500 mg/m^3) from 15.95 mg to 823.61 mg, but erosion is less important compared to rotor, which is well illustrated in Figure 14(b). The overall erosion rate is almost constant and has an average value of 3.47×10^{-2} mg/g. According to Table 1 and Figure 15(a), the reduction in blade length is from 1.96×10^{-5}% to 2.38×10^{-4}%, after one hour of sand ingestion for concentration between 10 and 500 mg/m^3. As seen in Figure 15(b), the blade chord at radius $R75$ is reduced from 2.197×10^{-3}% to 0.1183%, whereas that at tip is from 4.449×10^{-3}% to 0.1503%. Moreover, the thickness at radius $R75$ is reduced from 1.344×10^{-2}% to 0.8130%, whereas that at tip is from 3.621×10^{-2}% to 3.321%, as seen in Figure 15(c).

As exhibited in Figure 16, the erosion phenomenon is shown to distort the leading edge and reduce the chord and thickness of blade, progressively beyond 40% span till the tip. The process of erosion wear is clearer over the fore part of the suction side for all blade sections and the thickness is subsequently reduced and even more towards the tip section. Erosion damage is especially evident on the outboard sections of the rotor blades, where the tip approaches the sonic speed [1]. In addition, the distortion at leading edge affects the flow circulation and moves the stagnation point, which should alter the static pressure distribution and the aerodynamic

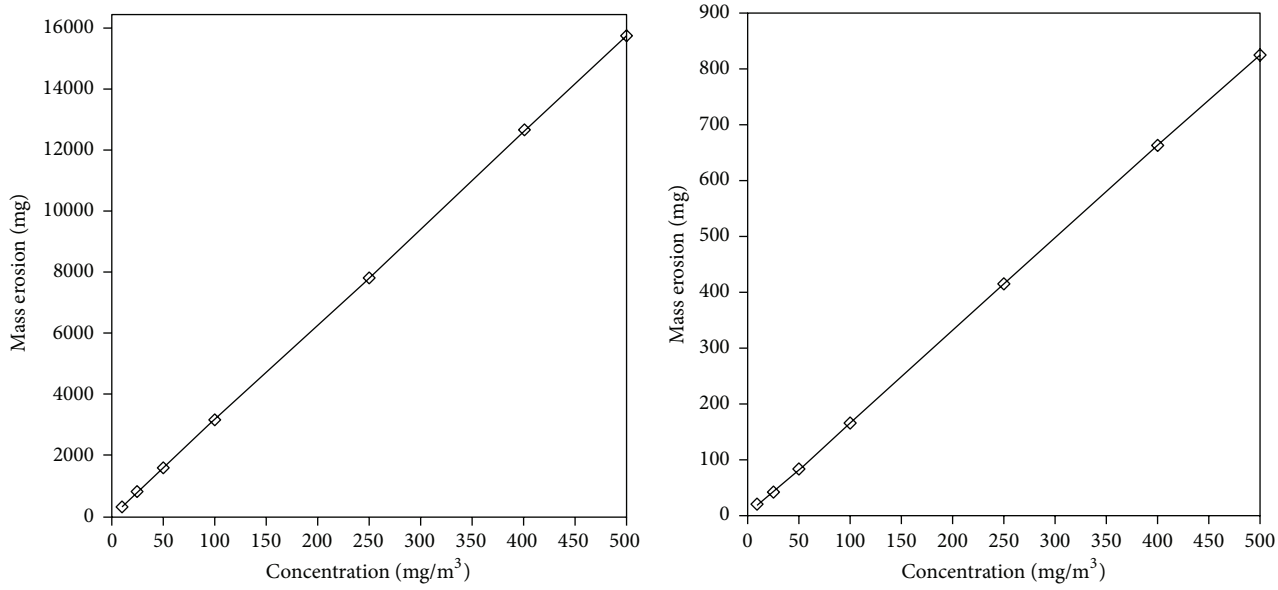

Figure 14: Mass erosion (mg) after one hour of sand ingestion: (a) blade and (b) spinner.

quality of the upper part of blade and subsequently the produced torque. As the maximum propeller thrust is obtained from 40% to 80% of blade span ($R40$–$R80$), there should be a subsequent drop in torque and performance coefficient to be evaluated in a next paper.

8. Conclusion

The present paper provides a reasonable insight into the particle dynamics and erosion of large blades propellers when exposed to different concentrations of sand particles. Tiny particles are shown to circulate around the rotor blade and stick to the flow path and also impact around the leading edge. Downstream of blade, these particles are deviated tangentially and follow helicoidal trajectories. When inertia of particles becomes more important, they deviate considerably from the flow path as a result of high drag and centrifugation. Many of these large particles impact the spinner and deflect to follow ballistic trajectories. At exit from rotor, they are deviated tangentially and projected upward, and many of them are entrained by the vortex and deviated downward. Multiple impacts are predicted around the blade leading edge due to its direct exposure to incoming particles and over suction side by particles arriving at high velocity and angle incidence. Extreme erosion area is revealed over the outer half of blade with blunting of the leading edge and thinning of the corner part of blade. As the maximum propeller thrust is expected to be from 40% to 80% of blade span, a subsequent drop in aerodynamic performance is related to this part. This information will in turn help to design propeller blades for minimum erosion and to envisage a coating for the critical regions with a hard material.

Nomenclature

A:	Area (m^2)
A_e:	Area of an element (m^2)
c:	Chord (m)
C:	Concentration (mg/m^3)
C_D:	Drag coefficient
C_L:	Lift coefficient
D:	Diameter of rotor (m)
d:	Diameter of particle (m)
e:	Thickness (m)
E:	Erosion rate (mg/g)
E_{eq}:	Equivalent erosion rate (mg/g/cm^2)
F:	Force (N)
h:	Length or height of blade (m)
k:	Turbulent kinetic energy (m^2/s^2)
K_1, K_2, K_3:	Material constants
l_e:	Dissipation length scale
m:	Mass (kg)
N_i:	Shape function
N_p:	Number of impacts on an element face
P:	Pressure (Pa)
r:	Radius, radial coordinate (m)
$R75$:	Radius at 75% of blade length
Re:	Reynolds number
t:	Time (s)
t_e:	Eddy lifetime (s)
U:	Peripheral velocity (m/s)
V:	Absolute velocity (m/s)
W:	Relative velocity (m/s)
z:	Axial coordinate (m)
x, y, z:	Cartesian coordinates.

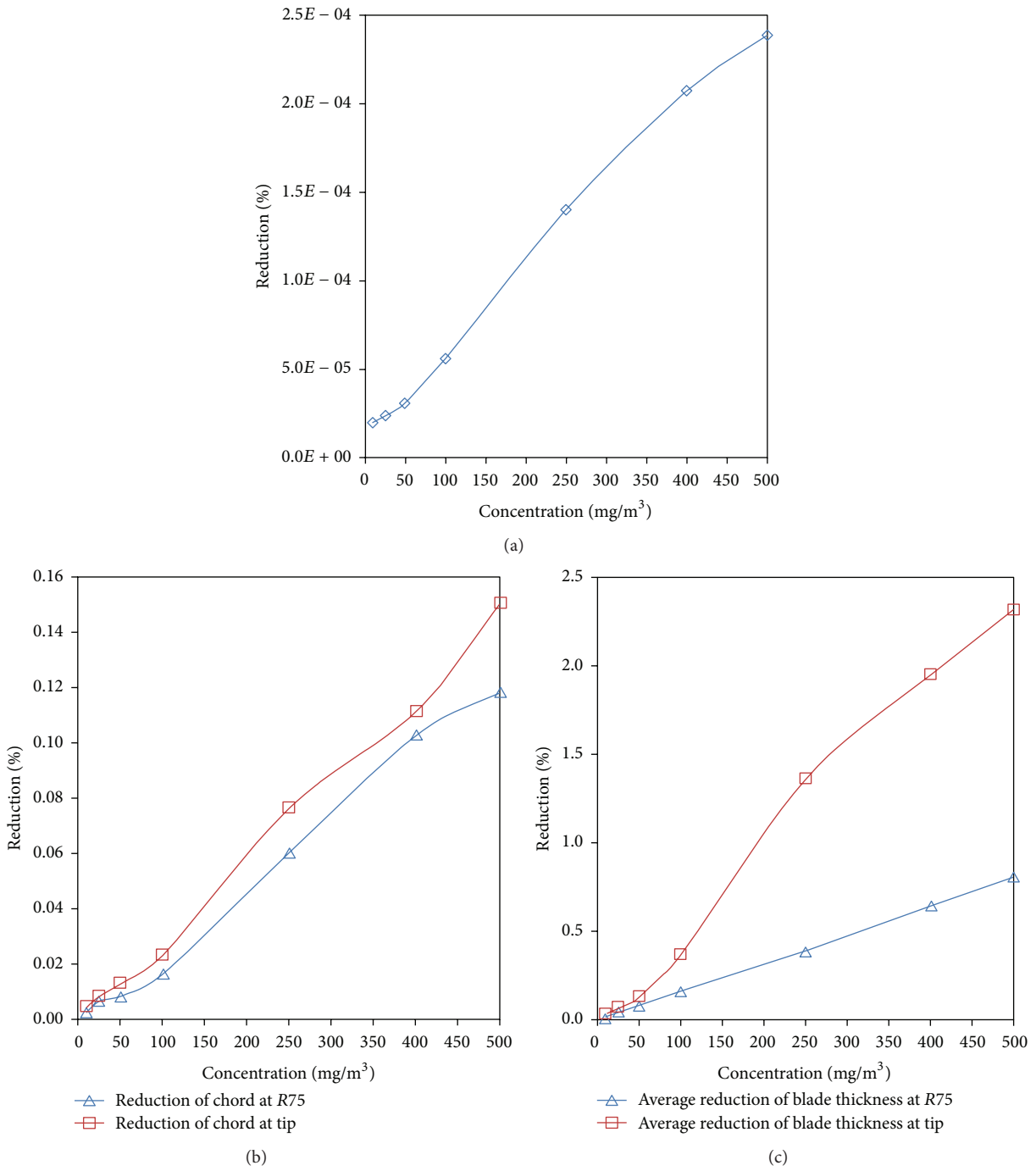

FIGURE 15: Blade geometry deteriorations with concentration after one hour of sand ingestion: (a) reduction of length, (b) reduction of chord, and (c) reduction of thickness.

Greek Letters

β: Impact angle (deg)
ε: Turbulence rate of dissipation (m^2/s^3)
ρ: Density (kg/m^3)
μ: Dynamic viscosity (kg/m·s)
ω: Speed of rotation (rad/s)
θ: Angular position (rad)
τ_p: Relaxation time (s).

Subscript

av: Average
D: Drag
f: Fluid
p: Particle
o: Related to maximum erosion
r: Radial
ϑ: Tangential component

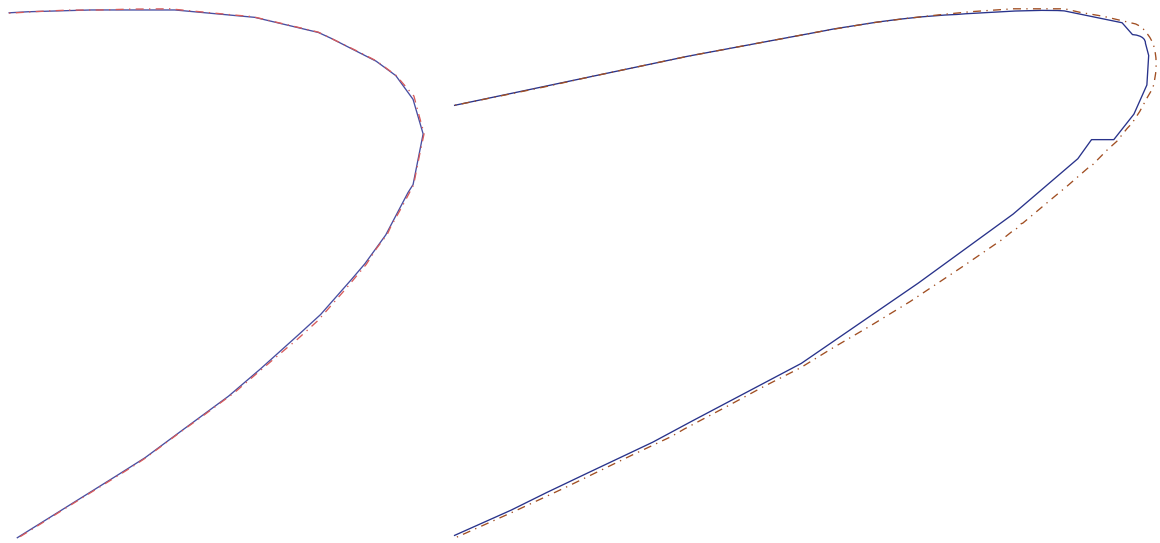

(a) (b)

Figure 16: Eroded profiles after one hour of sand ingestion of a concentration (500 mg/m^3): (a) *R*75 profile; (b) tip profile (dashed line is the initial profile and solid line is the eroded profile).

S: Saffman
z: Axial direction
1, 2: At impact and rebound from a surface.

Abbreviations

CFD: Computational fluid dynamics
RANS: Reynolds averaged Navier-Stokes
LPS: Linear profile scheme.

Conflict of Interests

The author declares no conflict of interests.

References

[1] T. Warren, S. C. Hong, C.-J. Yu, and E. L. Rosenzweig, "Enhanced erosion protection for rotor blades," in *Proceedings of the American Helicopter Society 65th Annual Forum*, pp. 2678–2686, Grapevine, Tex, USA, May 2009.

[2] P. Brotherhood and D. W. Brown, "Flight measurements of the effects of simulated leading-edge erosion on helicopter blade stall, torsional loads and performance," Reports and Memoranda 3809, R.A.E., Bedford, UK, 1976.

[3] W. Tabakoff, A. Hamed, and V. Shanov, "Blade deterioration in a gas turbine engine," *International Journal of Rotating Machinery*, vol. 4, no. 4, pp. 233–241, 1998.

[4] M. Morini, M. Pinelli, P. R. Spina, and M. Venturini, "Influence of blade deterioration on compressor and turbine performance," *ASME Journal of Engineering for Gas Turbines and Power*, vol. 132, no. 3, Article ID 032401, 11 pages, 2009.

[5] W. Sage and G. P. Tilly, "The significance of particles sizes in sand erosion of small gas turbines," *The Royal Aeronautical Society Journal*, vol. 73, pp. 427–428, 1969.

[6] M. F. Hussein and W. Tabakoff, "Dynamic behavior of solid particles suspended by polluted flow in a turbine stage," *Journal of Aircraft*, vol. 10, no. 7, pp. 434–440, 1973.

[7] M. F. Hussein and W. Tabakoff, "Computation and plotting of solid particle flow in rotating cascades," *Computers & Fluids*, vol. 2, no. 1, pp. 1–15, 1974.

[8] A. Hamed and S. Fowler, "Erosion pattern of twisted blades by particle laden flows," *Journal of Engineering for Power*, vol. 105, no. 4, pp. 839–843, 1983.

[9] A. Hamed and W. Tabakoff, "Experimental and numerical simulations of the effects of ingested particles in gas turbine engines," Tech. Rep. AGARD-CP-558, Erosion, Corrosion and Foreign Object Effects in Gas Turbines, 1994.

[10] G. P. Sallee, H. D. Kruckenburg, and E. H. Toomey, "Analysis of turbofan engine performance deterioration and proposed follow-on tests," Tech. Rep. NASA-CR-134769, 1978.

[11] C. Balan and W. Tabakoff, "Axial compressor performance deterioration," in *Proceedings of the 20th Joint Propulsion Conference*, vol. No of *AIAA Paper no. 84-1208*, Cincinnati, Ohio, USA, June 1984.

[12] A. Ghenaiet, R. L. Elder, and S. C. Tan, "Particles trajectories through an axial fan and performance degradation due to sand ingestion," in *Proceedings of the ASME Turbo Expo: Power for Land, Sea, and Air*, ASME Paper 2001-GT-0497, 12 pages, New Orleans, La, USA, June 2001.

[13] A. Ghenaiet, S. C. Tan, and R. L. Elder, "Numerical simulation of the axial fan performance degradation due to sand ingestion," in *Proceedings of the ASME Turbo Expo: Power for Land, Sea, and Air*, ASME Paper no. GT2002-30644, pp. 1181–1190, Amsterdam, The Netherlands, June 2002.

[14] A. Hamed, W. Tabakoff, and R. Wenglarz, "Erosion and deposition in turbomachinery," *AIAA Journal of Propulsion and Power*, vol. 22, no. 2, pp. 350–360, 2006.

[15] A. Ghenaiet, "Study of sand particle trajectories and erosion into the first compression stage of a turbofan," *Journal of Turbomachinery*, vol. 134, no. 5, Article ID 051025, 17 pages, 2012.

[16] M. Schrade, S. Staudacher, and M. Voigt, "Experimental and numerical investigation of erosive change of shape for high-pressure compressors," in *Proceedings of the ASME Turbo Expo: Turbine Technical Conference and Exposition*, ASME Paper GT2015-42061, 9 pages, Montreal, Canada, June 2015.

[17] CFX-TASCflow, Version 2.11, AEA Technology Engineering Software, Ltd. 2001.

[18] D. C. Wilcox, *Turbulence Modeling for CFD*, DCW Industries, La Canada, Calif, USA, 1994.

[19] D. C. Wilcox, "Simulation of transition with a two-equation turbulence model," *AIAA Journal*, vol. 32, no. 2, pp. 247–255, 1994.

[20] F. R. Menter, "Performance of popular turbulence models for attached and separated adverse pressure gradient flows," *AIAA Journal*, vol. 30, no. 8, pp. 2066–2072, 1992.

[21] F. R. Menter, "Improved two-equation k-ω turbulence model for aerodynamic flows," NASA TM-103975, 1992.

[22] A. Haider and O. Levenspiel, "Drag coefficient and terminal velocity of spherical and nonspherical particles," *Powder Technology*, vol. 58, no. 1, pp. 63–70, 1989.

[23] M. Sommerfeld, *Theoretical and Experimental Modeling of Particulate Flow—Overview and Fundamentals*, VKI Lecture Series, Von Karman Institute, Brussels, Belgium, 2000.

[24] D. J. Brown and P. Hutchinson, "The interaction of solid or liquid particles and turbulent fluid flow fields—a numerical simulation," *Journal of Fluids Engineering*, vol. 101, no. 2, pp. 265–269, 1979.

[25] J. S. Shirolkar, C. F. M. Coimbra, and M. Q. McQuay, "Fundamental aspects of modeling turbulent particle dispersion in dilute flows," *Progress in Energy and Combustion Science*, vol. 22, no. 4, pp. 363–399, 1996.

[26] A. D. Gosman and E. Ionnides, "Aspects of computer simulation of liquid fuelled combustors," in *Proceedings of the 19th Aerospace Science Meeting*, AIAA 81-0323, St. Louis, Mo, USA, January 1981.

[27] W. Tabakoff, A. Hamed, and D. M. Murugan, "Effect of target materials on the particle restitution characteristics for turbomachinery application," *Journal of Propulsion and Power*, vol. 12, no. 2, pp. 260–266, 1996.

[28] S. C. Tan and R. L. Elder, "Assessment of particle rebounds and fragmentation characteristics," Progress Report, Cranfield University, 1992.

[29] I. Finnie, "Erosion of surfaces by solid particles," *Wear*, vol. 3, no. 2, pp. 87–103, 1960.

[30] J. G. A. Bitter, "A study of erosion phenomena. Part II," *Wear*, vol. 6, no. 3, pp. 169–190, 1963.

[31] J. H. Neilson and A. Gilchrist, "Erosion by a stream of solid particles," *Wear*, vol. 11, no. 2, pp. 111–122, 1968.

[32] G. Grant and W. Tabakoff, "Erosion prediction in turbomachinery due to environmental solid particles," in *Proceedings of the 12th AIAA Aerospace Sciences Meeting*, AIAA Paper no. 74-16, Washington, DC, USA, January-February 1974.

[33] G. Grant and W. Tabakoff, "Erosion prediction in turbomachinery resulting from environmental solid particles," *AIAA Journal of Aircraft*, vol. 12, no. 5, pp. 471–478, 1975.

[34] G. Drensky, A. Hamed, W. Tabakoff, and J. Abot, "Experimental investigation of polymer matrix reinforced composite erosion characteristics," *Wear*, vol. 270, no. 3-4, pp. 146–151, 2011.